Force distributions in frictional granular media

Force distributions in frictional granular media

V. S. Akella,[1] M. M. Bandi,[1] H. George E. Hentschel,[2] Itamar Procaccia,[2] and Saikat Roy[2]

[1]*Collective Interactions Unit, OIST Graduate University, Onna, Okinawa, 904-0495 Japan*
[2]*Department of Chemical Physics, Weizmann Institute of Science, Rehovot 76100, Israel*

We report a joint experimental and theoretical investigation of the probability distribution functions (PDFs) of the normal and tangential (frictional) forces in amorphous frictional media. We consider both the joint PDF of normal and tangential forces together, and the marginal PDFs of normal forces separately and tangential forces separately. A maximum entropy formalism is utilized for all these cases after identifying the appropriate constraints. Excellent agreements with both experimental and simulation data are reported. The proposed joint PDF predicts giant slip events at low pressures, again in agreement with observations.

I. INTRODUCTION

In compressed frictional amorphous granular media the external pressure is balanced by normal and tangential (frictional) forces acting at the contacts between the grains [1]. The forces are very inhomogeneous, with a wide distribution of magnitude, resulting in the appearance of force chains which represent the largest forces which are percolating from wall to wall; see Fig. 1.

Intensive discussions of the nature of these interparticle forces and of their distributions in frictional amorphous media have been taking place for a number of decades. In 1995 Radjai and Roux [2] proposed that the probability distribution function (PDF) $P_1(F^{(n)})$ of the normal contact forces $F_{ij}^{(n)}$ between grains i and j has a different form for forces smaller or larger than the mean normal force $\langle F^{(n)} \rangle$:

$$P_1(F^{(n)}) \propto \left(\frac{F^{(n)}}{\langle F^{(n)} \rangle} \right)^{\alpha}, \quad F^{(n)} < \langle F^{(n)} \rangle, \qquad (1)$$

$$P_1(F^{(n)}) \propto \exp\left[\beta \left(1 - \frac{F^{(n)}}{\langle F^{(n)} \rangle} \right) \right], \quad F^{(n)} > \langle F^{(n)} \rangle. \qquad (2)$$

A similar expression was proposed for the PDF of the tangential frictional forces $F_{ij}^{(t)}$. A different expression was offered in the same year by the Chicago group [3]. This expression followed a theoretical model with the result

$$P_1(F^{(n)}) = \frac{k^k}{(k-1)!} \left(\frac{F^{(n)}}{\langle F^{(n)} \rangle} \right)^{k-1} \exp\left[-k \left(\frac{F^{(n)}}{\langle F^{(n)} \rangle} \right) \right]. \qquad (3)$$

As discussed by Thornton [4], this expression changes from an exponential distribution to an almost Gaussian distribution as the parameter k is varied from 1 to 12.

One year later, in 1996, Miller, O'Hern, and Behringer concluded on the basis of careful measurements that the model leading to Eq. (3) may miss important correlation effects, leading to disagreements with Eq. (3) [5]. In other words, these measurements indicated that a relevant PDF that needs to be studied is the joint PDF $P_2(F^{(n)}, F^{(t)})$. In fact, not much has

been reported in the literature about the effects of correlations between the normal and tangential forces. One of the aims of this paper is to close this gap.

A few years later, in 2000, Antony [6] noted that for values smaller than the average, the PDF of the normal forces can be fit with a "half Gaussian distribution" having four free parameters. For forces larger than the average the PDF was declared to be exponential. At larger values of the strain the PDF for forces smaller than the averages was found by Anthony to conform with a polynomial fit. One year later, in 2001, Blair *et al.* [7] found force distributions that "were well represented in all cases by the functional form":

$$P_1(F^{(n)}) = a\{1 - b \exp[-c(F^{(n)})^2]\} \exp[-d F^{(n)}], \qquad (4)$$

with a, b, c, and d being free parameters. Yet a few years later, in 2005, Corwin, Jaeger, and Nagel [8] offered a prediction that for Herzian contacts the PDF of the normal force should read

$$P_1(F^{(n)}) = \alpha \left[1 + (F^{(n)})^{2/3} \frac{\langle \Delta \rangle}{d} \right]^2 \exp\left[\frac{-\beta \left(F^{(n)} \right)^{5/3}}{\beta_0} \right], \qquad (5)$$

where $\langle \Delta \rangle$ is the average deformation of the granules. In the same year Majmudar and Behringer published their seminal paper in which they showed how to visualize the forces in frictional granular matter by using photoelastic disks [9]. They could show that the distributions of both the normal and the tangential forces (normalized by the mean normal force) depended on the type of external strain. The normal force distribution for the sheared system had a peak around the mean, a roughly exponential tail, and a dip towards zero for forces lower than the mean. In contrast, for isotropically compressed systems, the normal force distribution dipped towards zero for forces below the mean, was broad around the mean, and decayed faster for large forces compared to the sheared system. The tangential force distributions had a nearly exponential tail for forces larger than the mean for both the sheared and the isotropically compressed system.

The intervening years until the present time did not resolve the somewhat confusing status of the PDFs of the contact
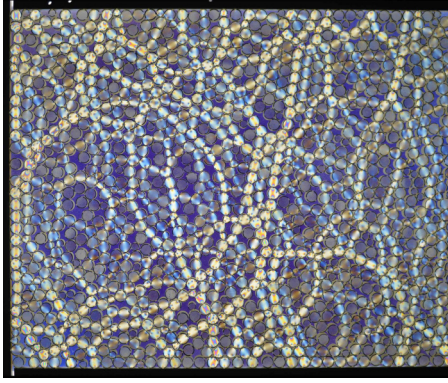
FIG. 1. A typical visualization of the force chains that hold together a compressed assembly of frictional granular photoelastic disks in two dimensions.

forces in frictional matter. An interesting line of attempts to nail down a solid prediction for these PDFs had employed the principle of maximum entropy subject to known constraints [10–13]. In some degree these attempts were motivated by the desire to define an "effective grain temperature." In the view of the present authors these attempts were somewhat rigid in following the example of statistical mechanics in trying to use the mean energy or the mean stress as the appropriate constraint (on top of normalization) under which the entropy is maximized. In statistical mechanics, as observed by Feynman [14], the only "legal" constraint is the mean energy since the predictions of the theory must be invariant to a redefinition of the zero-point energy E_0. The ratio of the probabilities to observe two states of energy E_1 and E_2, $\exp[(E_1 - E_2)/k_B T]$, must remain invariant to changes in the reference point E_0. If we added as a constraint, say, $\langle E^2 \rangle$, the exponential would include a quadratic term that were not invariant to changes in the zero point energy. This restriction is not relevant for the problem at hand. The forces between granules are naturally bounded by zero from below, and we can use any moment of the force distribution that appears appropriate. In this way we can reap the benefit of the information-theoretic meaning of the maximum entropy principle, providing us with the "least biased" prediction subject to measurable data [15,16]. In fact, we will show below that our measurements of the marginal PDF P_1 in both experiments and simulations agree very well with the predictions of maximal entropy subject to the mean and variance of the distributions. For the joint PDF P_2 one needs to add the correlation function that couples the normal and the tangential forces. In principle one could add additional moments as constraints, but we found the agreement with the data so good that this was (so far) deemed unnecessary.

To test the predictions of our approach we have measured the normal and tangential forces in frictional granular matter in both experiments and simulations. We start this paper in Sec. II by describing the experimental details and the resulting force measurements, together with similar measurements in numerical simulations. The next section, Sec. III, presents the maximum entropy approach; we calculate the predicted marginal PDFs of the magnitudes of the forces, both normal and tangential. In Sec. IV we compare the theoretical predictions to the results of experiments and numerical simulations.

In Sec. V we turn to the joint PDF P_2. We explain that the correlations between normal and tangential forces become particularly important at low pressure. There the theoretical PDFs predict a giant frictional slip when a compressed frictional assembly is decompressed. Simulation evidence for the existence of this giant slip is presented as well. Finally, Sec. VI offers a summary and some concluding remarks.

II. EXPERIMENTS AND NUMERICAL SIMULATIONS

In this section we present results of experiments and simulations in which both tangential and normal forces were measured. Here we focus on uniaxial straining and build the numerical simulations to mimic the experimental setup. The reader who is mainly interested in the resulting PDFs can jump directly to Sec. II C, in which these are presented.

A. Experimental information

1. Experimental setup

The schematic of the experimental setup is displayed in Fig. 2.comprises a chamber of inner dimensions 0.6 m in length, 1.1 m in width, and 0.02 m in height constructed from a steel frame with a transparent acrylic bottom plate. The chamber was lined with internal steel boundaries extending 5 cm into the chamber and connected with linear bearings that passed through the frame to rigid outer boundaries terminating in force sensors, thus setting effective inner chamber dimensions of 0.5 m length (L), 1 m width (W), and the height 0.02 m (H) kept unchanged. The two opposing boundaries along the
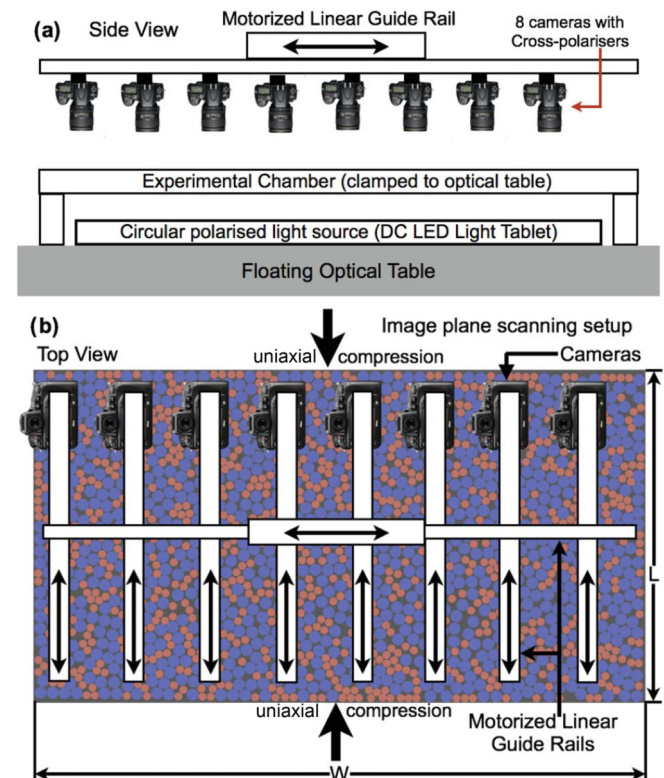

FIG. 2. Experimental schematic and image plane scanning setup: (a) side view; (b) top view.

L axis were movable and provided uniaxial compression [see Fig. 2(a)], whereas the transverse boundaries were held fixed. The chamber was rigidly clamped flat to an optical table on grade concrete flooring and floated with compressed air. A circular polarized dc light source (LED light tablet) was placed underneath the chamber to provide backlit illumination [see Fig. 2(b)]. The granular medium placed within the quasi-two-dimensional chamber consisted of a bidispersed set of photoelastic (birefringent response to stress) disks of diameters $D_L = 1.5$ cm for large and $D_S = 1$ cm for small disks. Full details of the quasistatic translation and boundary force detection methods are presented in Ref. [17].

2. Photoelastic disks

The photoelastic disks were made in-house by casting liquid polymer (SQ-2001 Epoxy Resin with SQ-3154 Hardener from Avipol, Brazil) in silicone molds (Shin-Etsu Silicones, Japan) in order to control both the modulus and friction coefficient of the photoelastic disks. The silicone mold base was maintained smooth, but the walls were intentionally designed to prescribed roughness to control the disk friction coefficient. The roughness was selected from an industrial standard sandpaper grit chart to transfer the sandpaper imprint onto the silicone mold, whose imprint in turn was transferred to disk walls during the polymer curing process. The disk bottom was left smooth to both avoid friction with the bottom acrylic plate as well as to permit clear transmission of light from the circular polarized backlit display. The resin-hardener mix poured into the silicone mold was baked with a free surface to allow for thermal expansion during the curing process and therefore avoid prestresses from developing within the disks. As a result, the resin-hardener mix poured into the molds formed a meniscus with mold walls and cured with an uneven top facet. The top faces of the cured photoelastic disks were ground on abrasive wheel to obtain clean facets with a final disk thickness of 0.975 cm.

The disk modulus was tuned by matching the epoxy resin and hardener mixture as well as the curing temperature: the curing process being exothermic, the curing temperature for the oven had to be determined by trial and error to obtain disks of desired moduli. Full details of the photoelastic materials methods will be presented in a separate article, but for disks employed in the present experiments the curing temperature was set fixed at 70 °C for a 24 h period, and the resin-hardener mix was changed to obtain two different elastic moduli of $E = 0.004$ GPa at friction coefficient $\mu = 0.27$ and $E = 0.4$ GPa at friction coefficient of $\mu = 0.4$. Since the friction coefficient resulting from a chosen roughness on the sandpaper grit chart is not known *a priori*, the friction coefficient was separately measured by the method explained in Ref. [18].

3. Imaging

A single digital still camera, no matter how high its resolution, does not provide the desired image quality for a quasi-two-dimensional granular configuration spanning 0.5 m × 1 m. We implemented an image plane scanning system (see Fig. 2 for schematic) so it could expressly meet two design criteria. First, the large system size renders any image susceptible to angular

distortions, commonly known as the fisheye effect. Whereas disks directly under the camera lens are viewed normal to the imaging plane, those farthest from the lens are at an oblique angle and do not appear as circular disks but as ellipsoids instead and lead to large errors in the detection of disk centers and contact stresses. Avoidance of the fisheye distortion demands moving the camera vertically higher, but it drastically reduces resolution of the acquired image because most of the imaged area extends outside the setup. Although disk centers are still identified by image analysis algorithms, fringe detection of the photoelastic stress measurement suffers considerably. Second, the high-precision quasistatic translation of 500 nm per quasistatic step achieved in this setup [17] demands disk displacement tracking of at least similar order. This requirement is not relevant for the current experiments as they involved a static configuration at a prescribed global pressure. Nonetheless, it becomes important for experimental analyses planned for the future.

In order to meet the above requirements, we constructed a scanning setup with eight Nikon D800E still photography cameras mounted in a row on motorized linear guide rails as shown in Fig. 2. The eight cameras scanned the image plane providing a set of images spanning sections of the entire configuration that were digitally stitched into a composite image of size $90\,000 \times 180\,000$ pixels. The composite image had an image resolution of 1.1 μm per pixel. Although not relevant in current experiments, further improvement in image resolution from 1.1 μm to 500 nm was achieved with subpixel interpolation using neighboring pixel intensity values. Finally, standard granular photoelastic experiments acquire two images [19,20], one without the circular cross-polarizer mounted on the camera lens for disk center detection and a second image with the cross-polarizer on for photoelastic fringe detection. Our setup acquires a single image with the circular cross-polarizer on, and both the disk center and photoelastic fringe detection are implemented in postprocessing analysis of acquired images in two separate passes as explained below.

4. Image analysis

The acquired composite image of the pack configuration was processed in two stages. Owing to backlit illumination, each disk has an illuminated ring along its edge due to diffraction bending of light with a sharp intensity gradient relative to photoelastic fringe signals which possess more gradual intensity gradients. In the first stage of image processing, we applied a high-pass Gaussian convolution filter thresholded against an intensity wave number (inverse of distance over which the diffraction-induced intensity gradient acts). Upon applying this filter, all wave numbers higher than the threshold wave number are retained in the image, and all wave numbers below it are removed. Ergo, the high-pass Gaussian convolution permits one to treat the disk edge diffraction-induced intensity as signal and photoelastic fringe intensity as noise in the first stage. We then applied a multiplicative variant of the standard (additive) circular Hough transform [18]. Knowledge of the total number of large and small disks and their respective radii in pixel units readily permits accurate detection of all disk centers.

In the second stage, we subtracted the high-pass Gaussian convoluted image of the first stage from the original image. The

resultant image now retains only photoelastic fringe intensities, which were then processed using the open source photoelastic grain solver algorithms [19,21] to obtain the normal and tangential forces at each stressed contact [9,22].

5. Experimental protocol

A total of 10 data sets were collected for a given modulus E and friction coefficient μ. Each of the 10 data sets represented a different initially prepared granular configuration. For each of those configurations, the system was quasistatically compressed in 500 nm steps and decompressed over 49 consecutive cycles. In the 50th compression cycle, the quasistatic compression was stopped once the boundary force sensors registered a boundary pressure value chosen *a priori*. For the experimental runs with disk material modulus $E = 0.004$ GPa and friction coefficient $\mu = 0.27$, the two-dimensional boundary pressure was chosen at $\mathcal{P} = 20$ N/m. For a second data set with disk material modulus $E = 0.1$ GPa and friction coefficient $\mu = 0.4$, the static two-dimensional global pressure was set at $\mathcal{P} = 76$ N/m for measurements. We note that the disks, especially ones with higher modulus, had a photoelastic threshold below which force values could not be reliably determined. Accordingly, our PDF does not include data on forces smaller than this threshold. This is a limitation of the experiments which needs to be taken into account when comparisons with theory are presented. The experimentally measured PDFs are displayed in Sec. II C.

B. Numerical simulations

Frictionless granular materials are commonly studied in quasistatic protocols involving conjugate gradient methods to bring the system to mechanical equilibrium after every straining step [23], but when the particles have friction, molecular dynamics simulations are preferred as they correctly keep track of both the normal and the (history-dependent) tangential forces [24]. So we set up simulation of uniaxial compression of two-dimensional granular packings, performed using open source codes, LAMMPS [25] and LIGGGHTS [26]. To mimic the experimental system the particles are taken as bidispersed disks of unit mass with diameters 1 and 1.4, respectively. All the lengths in the simulations are measured in units of the small diameter. The particles are placed randomly in a three-dimensional box of dimension 57 (along x), 102 (along y), and 1.4 (along z). Quasistatic compression is implemented by displacing the boundary particles. A side wall made of particles is placed in the direction perpendicular to the compression direction.

The contact forces (both the normal and tangential forces which arise due to friction) are modeled according to the discrete element method developed by Cundall and Strack [27]. When the disks are compressed they interact via both normal and tangential forces. Particles i and j, at positions r_i, r_j with velocities v_i, v_j and angular velocities ω_i, ω_j will experience a relative normal compression on contact given by $\Delta_{ij} = |r_{ij} - D_{ij}|$, where r_{ij} is the vector joining the centers of mass and $D_{ij} = R_i + R_j$; where R_i and R_j are respectively radius of particle i and j; this gives rise to a normal force $F_{ij}^{(n)}$. The normal force is modeled as a Hertzian contact, whereas the tangential force is given by a Mindlin force [27].

Defining $R_{ij}^{-1} \equiv R_i^{-1} + R_j^{-1}$, the force magnitudes are

$$F_{ij}^{(n)} = k_n \Delta_{ij} n_{ij} - \frac{\gamma_n}{2} v_{n_{ij}}, \quad F_{ij}^{(t)} = -k_t t_{ij} - \frac{\gamma_t}{2} v_{t_{ij}}, \quad (6)$$

$$k_n = k_n' \sqrt{\Delta_{ij} R_{ij}}, \quad k_t = k_t' \sqrt{\Delta_{ij} R_{ij}}, \quad (7)$$

$$\gamma_n = \gamma_n' \sqrt{\Delta_{ij} R_{ij}}, \quad \gamma_t = \gamma_t' \sqrt{\Delta_{ij} R_{ij}}. \quad (8)$$

Here Δ_{ij} and t_{ij} are normal and tangential displacement; R_{ij} is the effective radius. n_{ij} is the normal unit vector. k_n' and k_t' are spring stiffness for the normal and tangential mode of deformation; γ_n' and γ_t' are the viscoelastic damping constant for normal and tangential deformation. $v_{n_{ij}}$ and $v_{t_{ij}}$ are, respectively, the normal and tangential component of the relative velocity between two particles. The relative normal and tangential velocity are given by

$$v_{n_{ij}} = (v_{ij} \cdot n_{ij}) n_{ij}, \quad (9)$$

$$v_{t_{ij}} = v_{ij} - v_{n_{ij}} - \frac{1}{2}(\omega_i + \omega_j) \times r_{ij}, \quad (10)$$

where $v_{ij} = v_i - v_j$. Elastic tangential displacement t_{ij} is set to zero when the contact is first made and is calculated using $\frac{dt_{ij}}{dt} = v_{t_{ij}}$ and the rigid body rotation around the contact point is accounted for to ensure that t_{ij} always remains in the local tangent plane of the contact [28].

The translational and rotational acceleration of particles are calculated from Newton's second law; total forces and torques on particle i are given by

$$F_i^{(\text{tot})} = \sum_j F_{ij}^{(n)} + F_{ij}^{(t)}, \quad (11)$$

$$\tau_i^{(\text{tot})} = -\frac{1}{2} \sum_j r^{ij} \times F_{ij}^{(t)}. \quad (12)$$

The tangential force varies linearly with the relative tangential displacement at the contact point as long as the tangential force does not exceed the limit set by the Coulomb limit

$$F_{ij}^{(t)} \leqslant \mu F_{ij}^{(n)}, \quad (13)$$

where μ is a material-dependent coefficient. When this limit is exceeded the contact slips in a dissipative fashion. In our simulations we reset the value of t_{ij} so that $F_{ij}^{(t)} = 0.8\mu F_{ij}^{(n)}$. This choice is somewhat arbitrary but recommended on the basis of frictional slip events measured in experiments in the laboratory of J. Fineberg [29]. A global damping is implemented to reach the static equilibrium in a reasonable amount of time. After each compression step, a relaxation step is added so that the system reaches the static equilibrium, and then the forces at all the contacts are measured. In addition the global stress tensor is measured by taking averages of the dyadic products between the contact forces and the branch vector over all the contacts in a given area A:

$$\sigma_{\alpha\beta} = \frac{1}{A} \sum_{j \neq i} \frac{r_{ij}^\alpha F_{ij}^\beta}{2}. \quad (14)$$

The pressure $\mathcal{P}$ is determined from the trace of the stress. The resulting distribution of forces is presented in the next subsection.
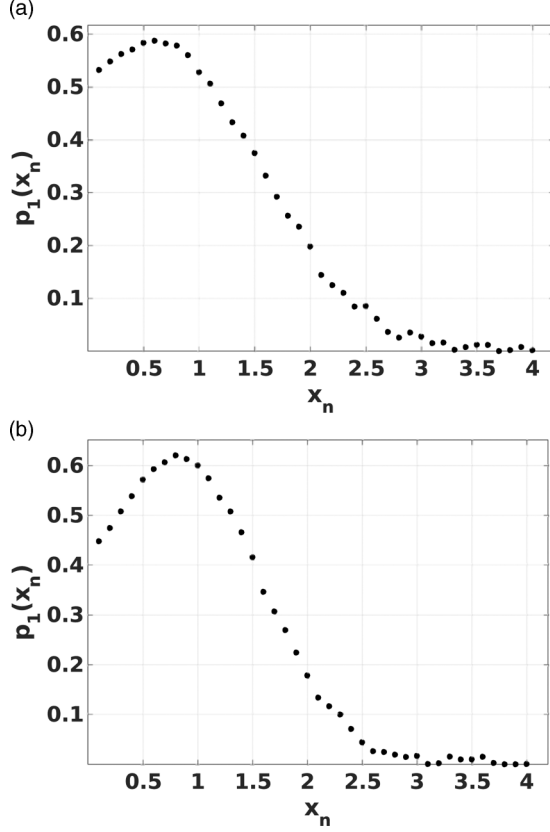
(a)

(b)

FIG. 3. The PDFs of the mean-normalized normal forces as measured in the experiment. (a) $\mu = 0.4$ and $\mathcal{P} = 76$ N/m. (b) $\mu = 0.27$ and $\mathcal{P} = 20$ N/m.
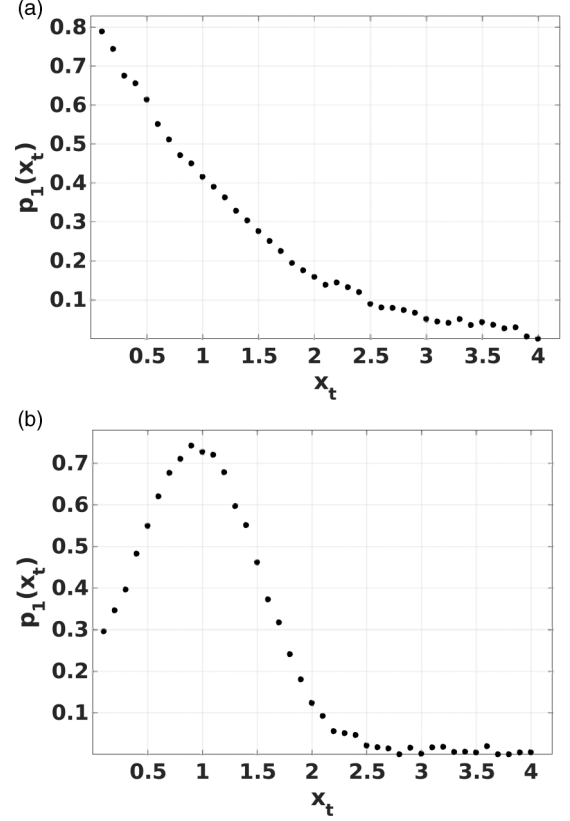
(a)

(b)

FIG. 4. The PDFs of the mean-normalized tangential forces as measured in the experiment. (a) $\mu = 0.4$ and $\mathcal{P} = 76$ N/m. (b) $\mu = 0.27$ and $\mathcal{P} = 20$ N/m.

C. The resulting normal and tangential force distributions

In discussing the force distributions one can consider in principle a number of different PDFs of varying complexity. As said in the introduction, the forces acting on the contacts of grains in frictional amorphous matter are highly inhomogeneous. Thus for N particles there exists a complex joint probability distribution $P_N(\{F^{(n)}\}, \{F^{(t)}\})$ for the magnitudes of these forces, where we have used the notation

$$\{F^{(n)}\} \equiv \left\{ F_{ij}^{(n)}; i, j \text{ running on all contacts} \right\} \quad (15)$$

for the normal forces, and similarly for the tangential forces. Integrating over all contacts except those for one pair of connected particles we can define the joint probability distribution $P_2(F^{(n)}, F^{(t)})$; while for the normal and transverse forces separately we can define the probability distribution for the normal forces:

$$P_1(F^{(n)}) = \int_0^\infty P_2(F^{(n)}, F^{(t)}) \, dF^{(t)}. \quad (16)$$

For the transverse forces

$$P_1(F^{(t)}) = \int_0^\infty P_2(F^{(n)}, F^{(t)}) \, dF^{(n)}. \quad (17)$$

In general $P_2(F^{(n)}, F^{(t)}) \neq P_1(F^{(n)}) P_1(F^{(t)})$. We will consider first the "single-particle" PDF P_1 for the normal and tangential forces. Later in Sec. V we will discuss also the joint PDF P_2.

1. Experimental results

In a number of experimental and simulation studies it was found that the probabilities $P_1(F^{(n)})$ and $P_1(F^{(t)})$ collapse nicely when plotted with the argument normalized by its mean. Accordingly we define

$$p_1(x_n) \equiv P_1\left(\frac{F^{(n)}}{\langle F^{(n)} \rangle}\right), \quad p_1(x_t) \equiv P_1\left(\frac{F^{(t)}}{\langle F^{(t)} \rangle}\right). \quad (18)$$

Here we present the PDFs $p_1(x_n)$ and $p_1(x_t)$, which were measured as explained in the experimental protocol above. In Fig. 3 find the PDFs of the normal forces at two different pressures $\mathcal{P} = 76$ N/m and $\mathcal{P} = 20$ N/m. The corresponding PDFs for the tangential mean-normalized forces are presented in Fig. 4.

It is interesting to note that the nature of the PDFs of the tangential forces is more sensitive to the change in parameters. The maximum which exists at both pressures for the PDF of the normal forces and for the tangential forces at low pressures is absent in the case of the tangential forces at high pressure.

2. Simulation results

Here we present the PDFs of the normal and tangential mean-normalized forces which were measured as explained in our discussion of the simulation. In Fig. 5 we present the PDFs of the mean-normalized normal forces, again for two different values of the pressure. The corresponding figures for the tangential mean-normalized forces are shown in Fig. 6. We
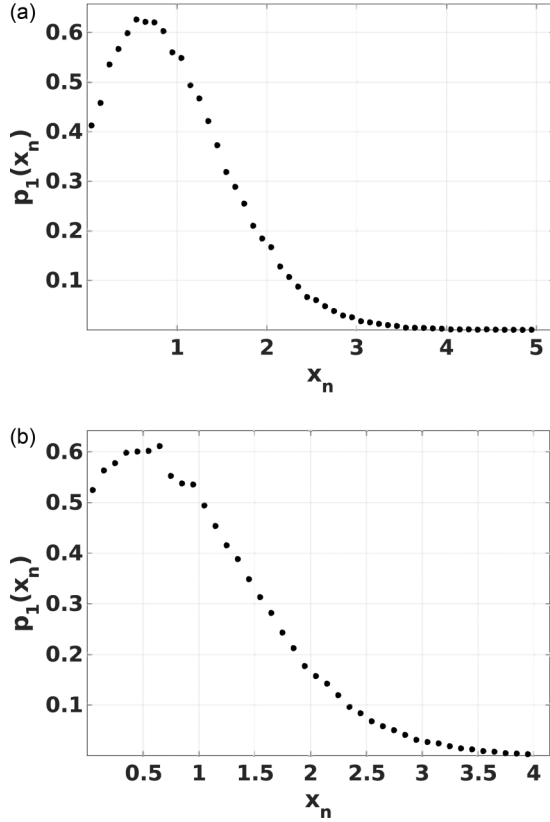
(a)

(b)

FIG. 5. The PDFs of the mean-normalized normal forces as measured in the simulations. (a) $\mu = 0.1$ and $\mathcal{P} = 83.5$. (b) $\mu = 0.1$ and $\mathcal{P} = 20$.

note that in the simulation results the PDFs of the tangential forces lack a maximum for both pressures.

III. MAXIMUM ENTROPY AND THE MARGINAL PDFS OF FORCE MAGNITUDES IN FRICTIONAL MATTER

We seek an analytic form for these PDFs by maximizing the entropy

$$S \equiv -\int_0^\infty p_1(x) \ln p_1(x)\,dx, \tag{19}$$

subject to constraints. Using a single constraint, that $\langle x \rangle = 1$, and normalizing the PDF in the range $[0,\infty]$ yields an exponential form for the distribution

$$p_1(x) = \lambda_a \exp(-\lambda_a x), \quad \text{(unacceptable)}, \tag{20}$$

for both the mean-normalized normal and tangential forces x_n and x_t. A glance at experimental data for the distributions of the mean-normalized normal and transverse forces in Figs. 3–6 shows that they are not exponential as Eq. (20) suggests. The existence of a clear maximum in the distributions indicates that a minimal additional constraint should be provided by the variance $\sigma^2 = \langle x^2 \rangle - \langle x \rangle^2$ in both cases. Using now the mean *and* the variance constraints, the maximum entropy formalism yields for both the normal and transverse forces similar forms for $p_1(x)$,

$$p_1(x) = \frac{\exp(-\lambda_a x - \lambda_b x^2)}{Z(\lambda_a, \lambda_b)}, \tag{21}$$
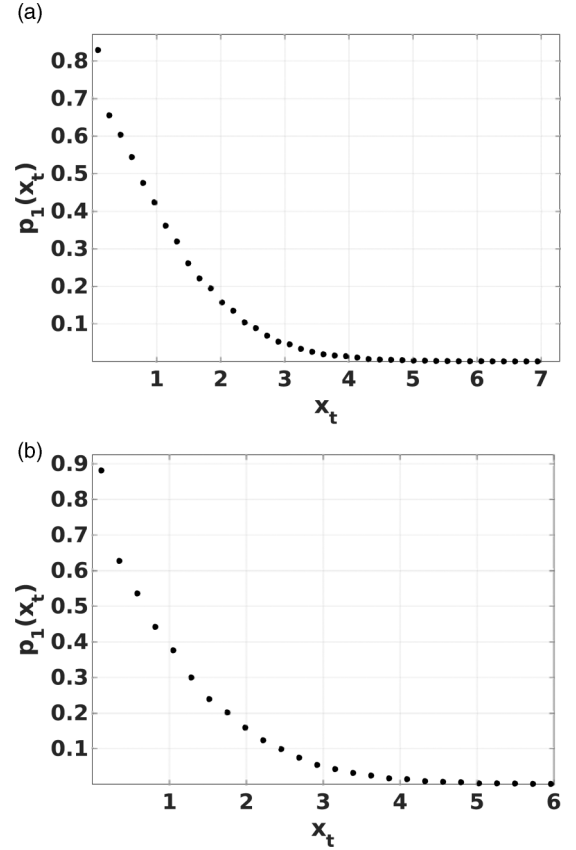
(a)

(b)

FIG. 6. The PDFs of the mean-normalized tangential forces as measured in the simulations. (a) $\mu = 0.1$ and $\mathcal{P} = 83.5$. (b) $\mu = 0.1$ and $\mathcal{P} = 20$.

with the partition function

$$Z(\lambda_a, \lambda_b) = \sqrt{\frac{\pi}{4\lambda_b}} e^{\frac{\lambda_a^2}{4\lambda_b}} \operatorname{erfc}\left(\frac{\lambda_a}{2\sqrt{\lambda_b}}\right). \tag{22}$$

The Lagrange multipliers can be found from the partial derivatives

$$-\frac{\partial \log Z(\lambda_a, \lambda_b)}{\partial \lambda_a} = 1,$$

$$-\frac{\partial \log Z(\lambda_a, \lambda_b)}{\partial \lambda_b} = 1 + \sigma^2. \tag{23}$$

To compute the Lagrange multipliers which are required to get explicit forms for the probability distributions let us define the associated functions $y = \lambda_a/(2\sqrt{\lambda_b})$. Then from Eqs. (23) we derive an equation for y as the nonlinear root of the equation

$$\frac{\left[y^2 + \frac{1}{2} - e^{-y^2}\frac{y}{\sqrt{\pi}\operatorname{erfc} y}\right]}{\left[-y + \frac{e^{-y^2}}{\sqrt{\pi}\operatorname{erfc} y}\right]^2} = 1 + \sigma^2. \tag{24}$$

Once we solve this last equation for $y(\sigma)$ we can find the two Lagrange multipliers that fix $p_1(x)$ as

$$\lambda_b(\sigma) = \left[-y(\sigma) + \frac{e^{-y^2(\sigma)}}{\sqrt{\pi}\operatorname{erfc} y(\sigma)}\right]^2,$$

$$\lambda_a(\sigma) = 2y(\sigma)\sqrt{\lambda_b(\sigma)}. \tag{25}$$

Finally we can now write the explicit distributions for both transverse forces $p_1(x_t)$ and the normal forces $p_1(x_n)$ as

$$p_1(x_t) = \frac{\exp\left(-\lambda_t x_t - \lambda_{tt} x_t^2\right)}{Z(\lambda_t, \lambda_{tt})},$$

$$p_1(x_n) = \frac{\exp\left(-\lambda_n x_n - \lambda_{nn} x_n^2\right)}{Z(\lambda_n, \lambda_{nn})}, \qquad (26)$$

with the partition functions

$$Z(\lambda_t, \lambda_{tt}) = \frac{\sqrt{\pi}}{4\lambda_{tt}} e^{\frac{\lambda_t^2}{4\lambda_{tt}}} \operatorname{erfc}\left(\frac{\lambda_t}{2\sqrt{\lambda_{tt}}}\right),$$

$$Z(\lambda_n, \lambda_{nn}) = \frac{\sqrt{\pi}}{4\lambda_{nn}} e^{\frac{\lambda_n^2}{4\lambda_{nn}}} \operatorname{erfc}\left(\frac{\lambda_n}{2\sqrt{\lambda_{nn}}}\right). \qquad (27)$$

IV. COMPARISON OF EXPERIMENTAL AND SIMULATION RESULTS TO THEORY

In this section we present the comparison of the theory to the measurements in experiments and in simulations. In executing this comparison we need to be careful. The theory assumes that we have full data for $0 \leqslant x \leqslant \infty$ and that the normalization is computed over the whole interval. As explained above, in the experiment we are limited in resolving the small forces due to the optical limitation, and very large forces suffer from lesser statistics. In the simulations we also recognize finite-size effects which limit the statistics of very small and very large

forces. Thus the measurement of the mean and variance of the PDFs directly from the data cannot conform with the theoretical requirement of having data over the full interval. To overcome this difficulty we have *fitted* the best values of the Lagrange multipliers using the data and the functional form Eq. (26). Once we fit the form we have a PDF over the whole interval, and we can compute the mean and the variance. We note that the mean and variance may deviate somewhat from their counterparts, which are evaluated directly from the data. We consider the latter to be inferior since they stem from incomplete data. We should recognize, however, that the definition of x_n and x_t involves the average forces, and therefore in the comparison below the x axes are rescaled somewhat differently to these axes in the PDFs shown so far. To ensure consistency, we always check whether the theoretical values of the Lagrange multipliers are indeed in agreement with the Eq. (25) using the recomputed average and variance. All the results below were obtained using this procedure and showed excellent self-consistency with the theoretical numbers.

In Fig. 7 we show the agreement between the theory and the experimental measurements of the PDFs of the mean-normalized normal forces. The corresponding comparisons for the PDFs of the mean-normalized tangential forces are shown in Fig. 8.

The comparison of the theory to the simulations results is shown next. In Fig. 9 we present the PDFs of the mean-normalized normal forces. Figures 9(a) and 9(b) correspond
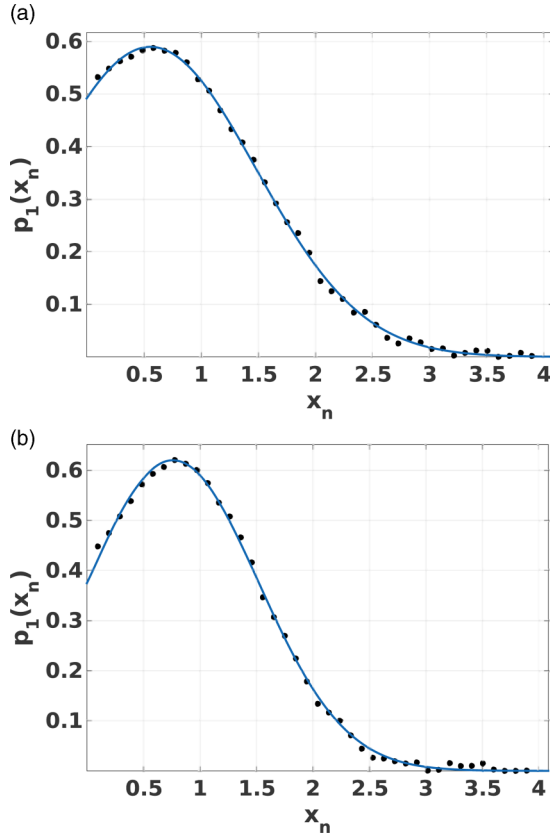

FIG. 7. Comparison of the functional prediction Eqs. (26) to the PDFs of the mean-normalized normal forces as measured in the experiments. Panels (a) and (b) correspond to Fig. 3. (a) $\lambda_n = -0.65$ and $\lambda_{nn} = 0.58$. (b) $\lambda_n = -1.32$ and $\lambda_{nn} = 0.87$.
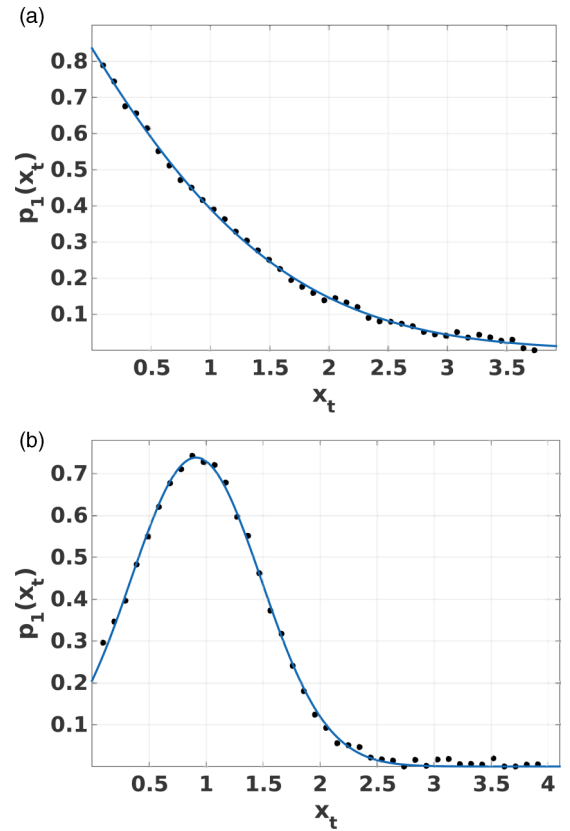

FIG. 8. Comparison of the functional prediction Eqs. (26) to the PDFs of the mean-normalized tangential forces as measured in the experiments. Panels (a) and (b) correspond to Fig. 4. (a) $\lambda_t = 0.64$ and $\lambda_{tt} = 0.11$. (b) $\lambda_t = -2.81$ and $\lambda_{tt} = 1.54$.
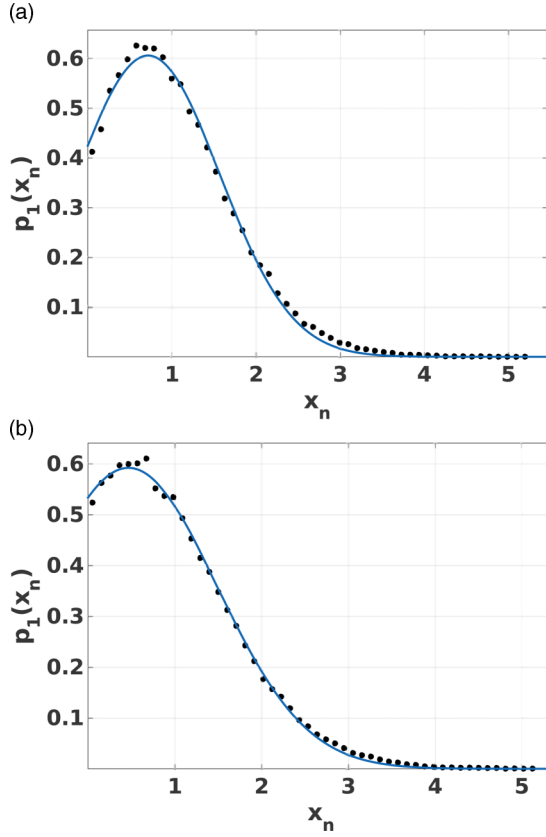
(a)

(b)

FIG. 9. Comparison of the functional prediction Eqs. (26) to the PDFs of the mean-normalized normal forces as measured in the simulations. Panels (a) and (b) correspond to Fig. 5. (a) $\lambda_n = -0.99$, $\lambda_{nn} = 0.69$. (b) $\lambda_n = -0.44$, $\lambda_{nn} = 0.48$.
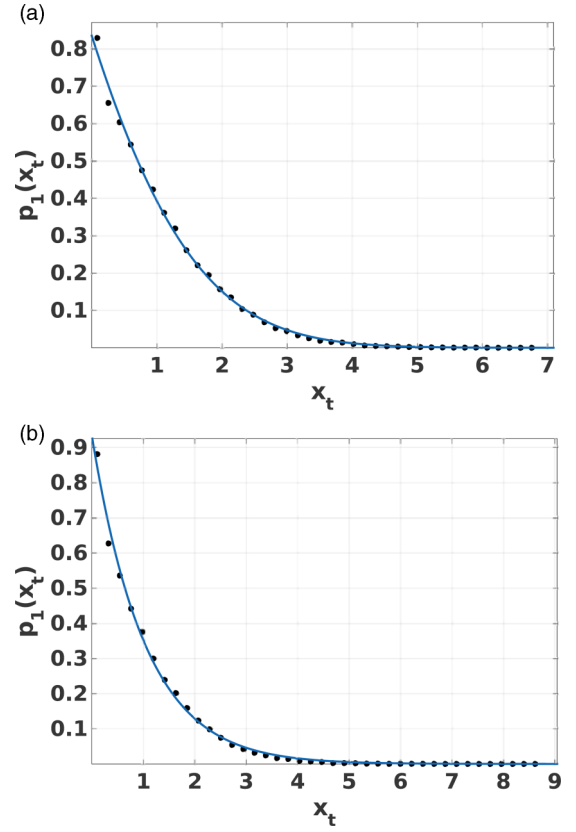
(a)

(b)

FIG. 10. Comparison of the functional prediction Eqs. (26) to the PDFs of the mean-normalized tangential forces as measured in the simulations. Panels (a) and (b) correspond to Fig. 6. (a) $\lambda_t = 0.65$, $\lambda_{tt} = 0.10$. (b) $\lambda_t = 0.96$, $\lambda_{tt} = 0.01$.

to Fig. 5. The corresponding comparisons for the PDFs of the mean-normalized tangential forces from the simulations are shown in Fig. 10. The conclusion is that at least for the data at hand, both in experiments and in simulations, at different values of the pressure, the theoretical prediction of the analytic forms of the $p_1(x_n)$ and $p_1(x_t)$ fit the data admirably well. We now turn to the joint probability $p_2(x_n, x_t)$, which is sensitive to the correlation between the normal and tangential forces. This will underline the predictive value of the present approach.

V. JOINT DISTRIBUTIONS AND THE PREDICTION OF A GIANT SLIP

In this section we study the properties of the joint distributions $p_2(x_n, x_t)$ as a function of the pressure. As had been commented in Ref. [5], correlations between the normal and tangential forces cannot be neglected with impunity. If there were no correlations between the normal and tangential

forces, then we could expect that $\langle x_n x_t \rangle = 1$ at all pressures. Measuring these correlations in the simulations shows that this is not the case at *any* pressure. We therefore need to take these correlations into account, expose the physical reason for the correlations, and draw the necessary conclusions. We will argue in this section that the fundamental reason for the correlation is the Coulomb constraint (13). The most important consequence that we could find is the existence of a giant slip event at low pressures as described and discussed below.

A. Maximum entropy formalism for the joint distributions

In order to employ the maximum entropy formalism for the joint distributions we need to incorporate the correlation $\langle x_n x_t \rangle$ into the formalism. Measuring this correlation in either experiments or simulations and introducing an additional lagrange multiplier $\lambda_c(\mathcal{P})$ we can write the maximum entropy joint distribution

$$p_2(x_n, x_t) = \frac{\exp\left[-\lambda_n x_n - \lambda_{nn} x_n^2 - \lambda_t x_t - \lambda_{tt} x_t^2 - \lambda_c x_n x_t\right]\theta(\mu\langle F^n \rangle x_n - \langle F^t \rangle x_t)}{Z_2}, \tag{28}$$

where the θ function is respecting the Coulomb constraint and

$$Z_2 = \int_0^\infty \int_0^\infty dx_n \, dx_t \exp\left[-\lambda_n x_n - \lambda_{nn} x_n^2 - \lambda_t x_t - \lambda_{tt} x_t^2 - \lambda_c x_n x_t\right]\theta(\mu\langle F^n \rangle x_n - \langle F^t \rangle x_t). \tag{29}$$

The new Lagrange multiplier λ_c can now be extracted from the additional equation

$$-\partial \log Z_2(\lambda_n, \lambda_{nn}, \lambda_t, \lambda_{tt}, \lambda_c)/\partial \lambda_c = \langle x_n x_t \rangle. \qquad (30)$$

In reality it turns out that Eqs. (29) and (30) are somewhat difficult to invert to get an explicit expression for the five pressure-dependent Lagrange multipliers $\lambda_n(\mathcal{P}), \lambda_{nn}(\mathcal{P}), \lambda_t(\mathcal{P}), \lambda_{tt}(\mathcal{P}), \lambda_c(\mathcal{P})$. For a precise calculation all these are required as the joint distribution has altered in form from our marginal expressions. At this point we are interested, however, in the *qualitative* predictions that the formalism can provide. To this aim we shall keep the four lagrange multipliers given by Eqs. (25) for the marginal distributions, and neglect first all correlations between the normal and tangential forces. Then we can expand the partition function in powers of λ_c to second order. In this approximation the normal and tangential terms become disconnected, and we can write

$$Z_2 \approx Z_n Z_t \left[1 - \lambda_c \langle x_n x_t \rangle_0 + (1/2)\lambda_c^2 \langle x_n^2 x_t^2 \rangle_0 + \cdots \right], \quad (31)$$

where a subscript zero means the lowest order approximation of no correlation. Now in this approximation $\langle x_n x_t \rangle_0 \approx \langle x_n \rangle \langle x_t \rangle = 1$ and $\langle x_n^2 x_t^2 \rangle_0 \approx \langle x_n^2 \rangle \langle x_t^2 \rangle$ and using Eq. (30), we find

$$\langle x_n x_t \rangle = \frac{1 - \lambda_c \langle x_n^2 \rangle \langle x_t^2 \rangle}{1 - \lambda_c + (1/2)\lambda_c^2 \langle x_n^2 \rangle \langle x_t^2 \rangle}. \qquad (32)$$

Equation (32) can be solved to get λ_c in terms of the known second moments of the normal and tangential forces

$$\lambda_c \approx \left[1/(\langle x_n^2 \rangle \langle x_t^2 \rangle) - 1/\langle x_n x_t \rangle \right]$$
$$+ \sqrt{\left[1/\langle x_n x_t \rangle^2 - 1/(\langle x_n^2 \rangle \langle x_t^2 \rangle)^2 \right]}. \qquad (33)$$

Using our simulations data we evaluated $\lambda_c(\mathcal{P})$ for any desired pressure. We found that $\lambda_c(\mathcal{P})$ is a weak function of pressure but clearly nonzero in value.

B. Predictions

We are now in a position to find the joint probability $P_2(F^{(n)}, F^{(t)})$ at different pressures from Eqs. (28) and (29). Plotting the resulting joint PDFs results in a very interesting observation: as the pressure decreases a singularity in the distribution starts to appear at low pressures (see Fig. 11). In addition the $F^{(n)}, F^{(t)}$ axes contract (since the mean forces are proportional to the pressure). It appears that the joint probability diverges near $F^{(n)} = 0, F^{(t)} = 0$ as $P_2(0,0;\mathcal{P}) \propto 1/\mathcal{P}^2$. The singular behavior can be seen more directly in the variable $Y = F^{(t)} - \mu F^{(n)}$. In Fig. 12 we have plotted $P_Y(F^{(t)} - \mu F^{(n)}; \mathcal{P})$, which can be found directly from the definition

$$P_Y(F^{(t)} - \mu F^{(n)}; \mathcal{P})$$
$$= \int_0^\infty \int_0^\infty dF^{(n)} dF^{(t)} P_2(F^{(n)}, F^{(t)}; \mathcal{P}) \delta(F^{(t)} - \mu F^{(n)}),$$

$$(34)$$

for $\mathcal{P} = 0.27$. It is clear that a singularity is growing at $Y = 0$.
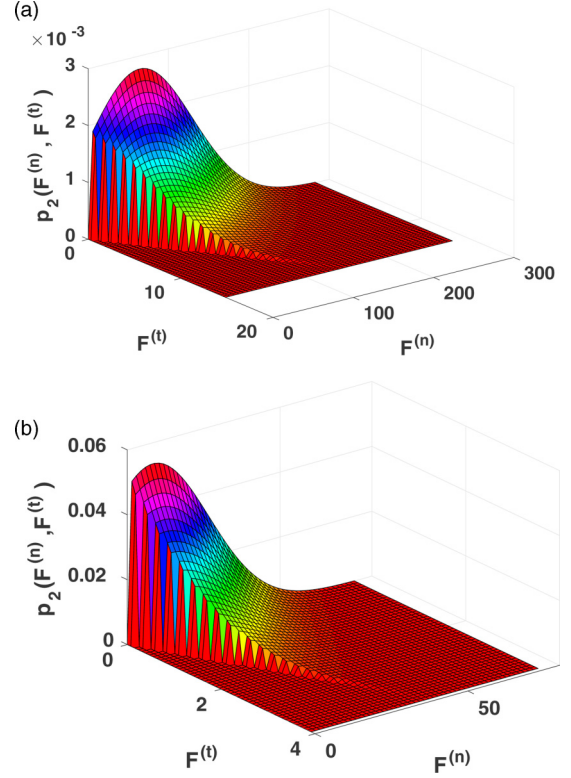
(a)

(b)

FIG. 11. Plot of the joint probability $P_2(F^{(n)}, F^{(t)})$ versus $F^{(n)}, F^{(t)}$ for $\mathcal{P} = 83.5$ (a) and $P_2(F^{(n)}, F^{(t)})$ versus $F^{(n)}, F^{(t)}$ for $\mathcal{P} = 20$ (b). Note the early appearance of a singularity at small values of $F^{(n)}, F^{(t)}$ at the lower pressures. Note also the very different scales required to plot $P_2(F^{(n)}, F^{(t)})$ at high and low pressures. The sharp drop in probability is due to the Coulomb constraint; cf. Eq. (28).

C. Validation and consequences

The maximum entropy formalism predicts an interesting and revealing aspect of the joint PDFs, hidden in their pressure dependence. To flush out this aspect we show in Fig. 13 the PDFs $p_1(x_n)$ and $p_1(x_t)$ obtained in simulations for the low pressure $\mathcal{P} = 0.27$. Besides the obvious remark that the maximum entropy forms fit the data very well also at this
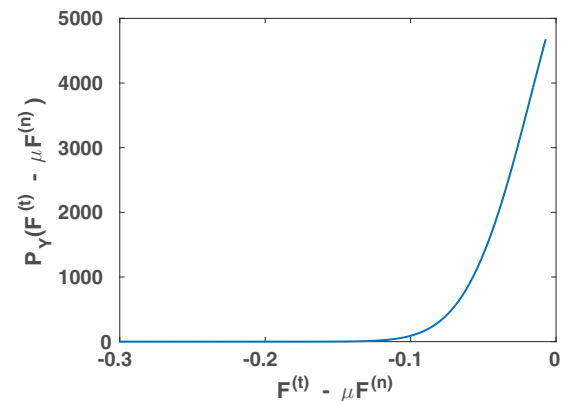

FIG. 12. Plot of the probability distribution for the variable $Y = F^{(t)} - \mu F^{(n)}$ given by $P_Y(Y; \mathcal{P} = 0.27)$ versus Y for $\mathcal{P} = 0.27$ supporting the notion that a singularity appears at low pressures.
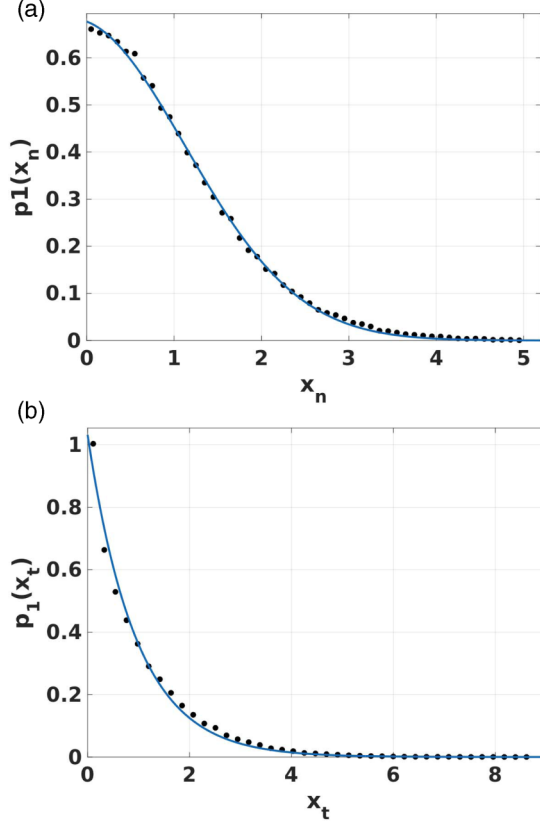
FIG. 13. The PDFs of the mean-normalized normal and tangential forces as measured in the simulations for the low pressure $\mathcal{P} = 0.27$. (a) $\lambda_n = 0.1$, $\lambda_{nn} = 0.28$; (b) $\lambda_t = 0.97$, $\lambda_{tt} = 0.01$.

very low pressure, we can now see the systematics in $p_1(x_n)$ as a function of the pressure. Comparing Figs. 9(a), 10(a), and 13(a), we can see that the probability to find *small* normal forces is increasing when the pressure decreases. We even lose at $\mathcal{P} = 0.27$ the maximum in $p_1(x_n)$ which is so prominent at higher pressures. But this means that when the pressure decreases there can be a higher probability to bust the Coulomb conditions Eq. (13). Accordingly, we can expect that decreasing the pressure may result in large frictional slip events. As argued in the last subsection, the best way to examine this possibility is to use our numerics to compute the probability distribution function $P(F_{ij}^{(t)} - \mu F_{ij}^{(n)})$. we display this function for varying pressures in Fig. 14. We observe the tendency of the PDF to exhibit a singularity near zero when the pressure decreases. This is a strong indication that when we approach $\mathcal{P} = 0$ we should expect a giant frictional slip event that is connected to the presence of an "unjamming" singularity.

To test this prediction we focus now on a typical decompression protocol and ask how many frictional slip events $\mathcal{N}_s$ occur while we decompress from the maximal pressure to any given pressure $\mathcal{P}$. In other words, we measure

$$\mathcal{N}_s(N, \mathcal{P}_{\max}, \mathcal{P}) \equiv \int_{P}^{\mathcal{P}_{\max}} n(N, \mathcal{P}) \, d\mathcal{P}, \quad (35)$$
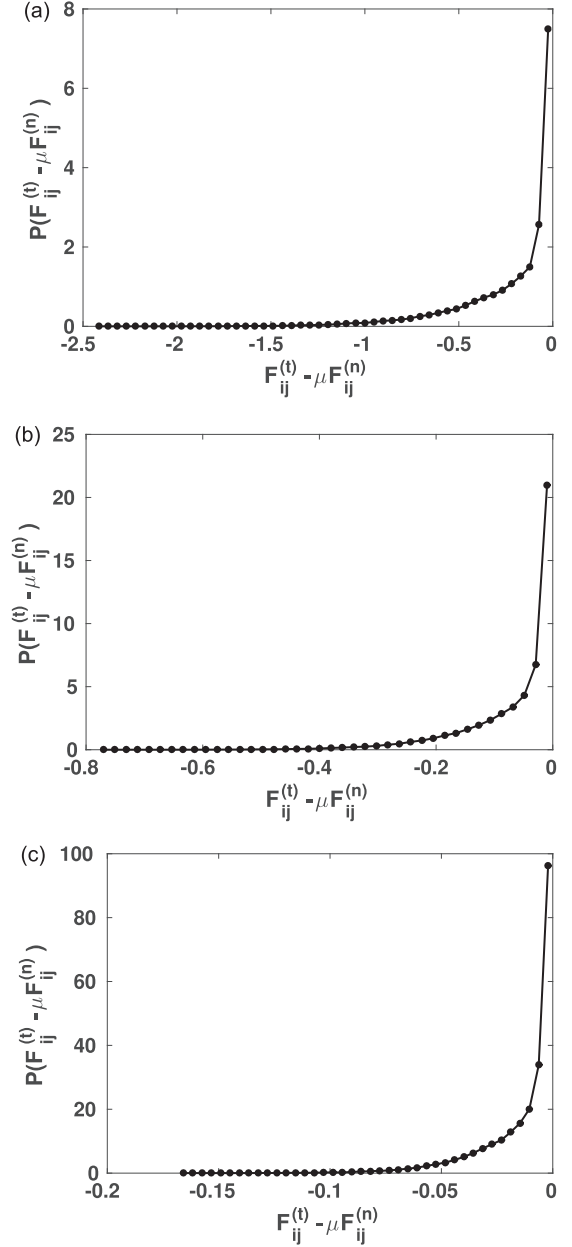

FIG. 14. The PDF $P(F_{ij}^{(t)} - \mu F_{ij}^{(n)})$ for varying pressures. (a) $\mathcal{P} = 5$; (b) $\mathcal{P} = 1$; (c) $\mathcal{P} = 0.27$. Note the scale and the tendency for a singularity near zero when the pressure decreases.

where $n(N, \mathcal{P}) \, d\mathcal{P}$ are the number of frictional slips that occur when decompressing from $\mathcal{P} + d\mathcal{P}$ to $\mathcal{P}$:

$$n(N, \mathcal{P}) \equiv -\frac{d\mathcal{N}_s(N, \mathcal{P}_{\max}, \mathcal{P})}{d\mathcal{P}}. \quad (36)$$

The result of the measurement of $\mathcal{N}_s(N, \mathcal{P}_{\max}, \mathcal{P})$ as a function of $\mathcal{P}$ is shown in Fig. 15. The simulation indicates an apparent divergence of the cumulative number of slip events as the pressure decreases towards zero.

The quantitative theoretical understanding of the divergence of the cumulative slips will be described in a later publication.
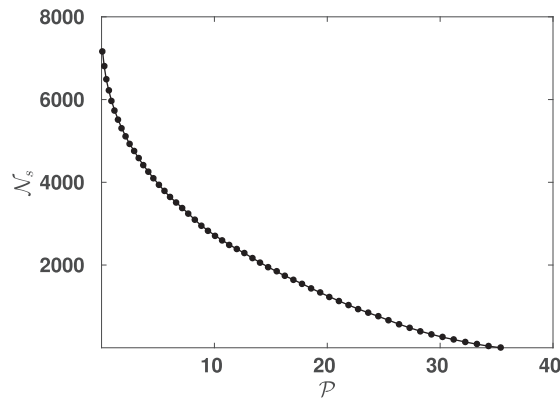
FIG. 15. The cumulative number of frictional slips $\mathcal{N}_s(N, \mathcal{P}_{max}, \mathcal{P})$ as a function of P averaged over 10 independent decompression legs. The maximal pressure $\mathcal{P}_{max}$ averaged over these 10 legs is $\mathcal{P}_{max} = 35.4$ and $N = 4000$. Note the apparent divergence of the cumulative number when the pressure decreases to zero.

considered pressures. The fits were excellent when the PDFs exhibited maxima as well as when maxima were absent. For the marginal PDFs two Lagrange multipliers were called for, and five were necessary for the joint PDFs. Thus the mean and variance of the distributions were also sufficient to provide the necessary Lagrange multipliers. In addition to reporting the useful descriptive nature of the functional forms provide by the maximum entropy formalism, we also presented their predictive usefulness. The formalism generated joint PDFs with increasing singularity towards low pressure. This singularity indicated that giant frictional slips are expected close to unjamming. Simulations supported fully this prediction.

It would be useful in the future to examine the predictions of the maximum entropy formalism in situations of different external strains such as shear and oscillations. Taking into account the quality of the fits presented above and the predictiveness of the resulting PDFs it seems worthwhile to examine the range of applicability in both experiments and simulations.

VI. CONCLUDING REMARKS

In conclusion, we considered the PDFs for the magnitudes of normal and tangential forces in frictional granular matter, focusing on the marginal and joint distribution $P_1(F^{(n)})$, $P_1(F^{(t)})$, and $P_2(F^{(n)}, F^{(t)})$. We showed that the maximum entropy formalism provides a very adequate functional form for these PDFs in both experiment and simulations at all the

ACKNOWLEDGMENTS

[1] O. Gendelman, Y. G. Pollack, I. Procaccia, S. Sengupta, and J. Zylberg, Phys. Rev. Lett. **116**, 078001 (2016).

[2] F. Radjai and S. Roux, Phy. Rev E **51**, 6177 (1995).

[3] C.-H. Liu, S. R. Nagel, D. A. Schecter, S. N. Coppersmith, S. Majumdar, O. Narayan, and T. A. Witten, Science **269**, 513 (1995).

[4] C. Thornton, KONA Powder Part. J. **15**, 81 (1997).

[5] B. Miller, C. O'Hern, and R. P. Behringer, Phys. Rev. Lett. **77**, 3110 (1996).

[6] S. J. Antony, Phys. Rev. E **63**, 011302 (2000).

[7] D. L. Blair, N. W. Mueggenburg, A. H. Marshall, H. M. Jaeger, and S. R. Nagel, Phys. Rev. E **63**, 041304 (2001).

[8] E. I. Corwin, H. M. Jaeger, and S. R. Nagel, Nature (London) **435**, 1075 (2005).

[9] T. S. Majmudar and R. P. Behringer, Nature (London) **435**, 1079 (2005).

[10] M. Shahinpoor, Powder Technol. **25**, 163 (1980).

[11] K. Bagi, Granular Matter **5**, 45 (2003).

[12] J. D. Goddard, Int. J. Solids and Sturctures **41**, 5851 (2004) and references therein.

[13] S. Henkes, C. S. O'Hern, and B. Chakraborty, Phys. Rev. Lett. **99**, 038002 (2007).

[14] R. P. Feynman, *Statistical Mechanics: A Set of Lectures* (Benjamin, Reading, MA, 1972).

[15] C. E. Shannon and W. Weaver, *The Mathematical Theory of Communication* (University of Illinois Press, Urbana, 1964).

[16] R. D. Levine and M. Tribus, editors, *The Maximum Entropy Formalism* (MIT Press, Cambridge, MA, 1979).

[17] M. M. Bandi, H. G. E. Hentschel, I. Procaccia, S. Roy, and J. Zylberg, Europhys. Lett. **122**, 38003 (2018).

[18] M. M. Bandi, M. K. Rivera, F. Krzakala, and R. E. Ecke, Phys. Rev. E **87**, 042205 (2013).

[19] K. E. Daniels, J. E. Kollmer, and J. G. Puckett, Rev. Sci. Instrum. **88**, 051808 (2017).

[20] N. Iikawa, M. M. Bandi, and H. Katsuragi, Phys. Rev. Lett. **116**, 128001 (2016).

[21] https://github.com/jekollmer/PEGS.

[22] T. S. Majmudar, Ph.D. thesis, Duke University (2006).

[23] T. G. Mason, M.-D. Lacasse, G. S. Grest, D. Levine, J. Bibette, and D. A Weitz, Phys. Rev. E **56**, 3150 (1997).

[24] O. Gendelman, Y. G. Pollack, and I. Procaccia, Phys. Rev. E **93**, 060601(R) (2016).

[25] S. Plimpton, J. Comput. Phys. **117**, 1 (1995).

[26] C. Kloss, C. Goniva, A. Hager, S. Amberger, and S. Pirker, Prog. Comput. Fluid Dyn. **12**, 140 (2012).

[27] P. Cundall and O. Strack, Geotechnique **29**, 47 (1979).

[28] L. E. Silbert, D. Ertas, G. S. Grest, T. C. Halsey, D. Levine, and S. J. Plimpton, Phys. Rev. E **64**, 051302 (2001).

[29] J. Fineberg (private communication).